Geophysical Journal International

Geophys. J. Int. (2014) **196,** 612–625
Advance Access publication 2013 October 23

doi: 10.1093/gji/ggt401

Seismic event distributions and off-fault damage during frictional sliding of saw-cut surfaces with pre-defined roughness

T. H. W. Goebel,[1] T. Candela,[2] C. G. Sammis,[1] T. W. Becker,[1] G. Dresen[3] and D. Schorlemmer[3]

[1]*University of Southern California, Department of Earth Sciences,* 90089*, Los Angeles, CA, USA. E-mail:* thw.goebel@gmail.com
[2]*Pennsylvania State University, Department of Geosciences,* 16802*, University Park, PA, USA*
[3]*German Research Centre for Geosciences, Geodynamics and Geomaterials, D-*14473*, Potsdam, Germany*

Accepted 2013 September 30. Received 2013 August 12; in original form 2013 June 12

GJI Seismology

SUMMARY

The motion along upper crustal faults in response to tectonic loading is controlled by both loading stresses and surface properties, for example, roughness. Fault roughness influences earthquake slip distributions, stress-drops and possible transitions from stable to unstable sliding which is connected to the radiation of seismic energy. The relationship between fault roughness and seismic event distributions is insufficiently understood, in particular, the underlying mechanisms of off-fault seismicity creation in the proximity of rough faults are debated. Here, we investigate the connection between roughness and acoustic emission (AE) density with increasing fault-normal distance during loading of surfaces with pre-defined roughness. We test the influence of fault roughness and normal stress variations on the characteristics of AE off-fault distributions. To this end, two sets of experiments were conducted: one to investigate the influence of initial surface roughness at constant confining pressure, and the other to investigate the influence of fault-normal stresses at constant roughness. Our experiments reveal a power-law decay of AE density with distance from the slip surface. The power-law exponents are sensitive to both fault roughness and normal stress variations so that larger normal stresses and increased roughness lead to slower AE density decay with fault-normal distance. This emphasizes that both roughness and stress have to be considered when trying to understand microseismic event distributions in the proximity of fault zones. Our results are largely in agreement with theoretical studies and observations of across-fault seismicity distributions in California suggesting a connection between off-fault seismicity and fault roughness over a wide range of scales. Seismicity analysis including a possible mapping between off-fault activity exponents, fault stresses and roughness, can be an important tool in understanding the mechanics of faults and their seismic hazard potential.

Key words: Statistical seismology; Rheology and friction of fault zones; Dynamics and mechanics of faulting; Fractures and faults.

1 INTRODUCTION

Much of the deformation at tectonic plate boundaries is focused within zones of relative weakness, that is, faults. Fault zones accumulate strain over time and release it over a spectrum of slip events of different size and velocity (e.g. Peng & Gomberg 2010). The characteristics of these slip events may be a function of fault roughness over a range of scales (e.g. Chester & Chester 2000; Dieterich & Smith 2009; Candela *et al.* 2011a,b). The roughness of natural fault zones varies from the subgrain scale (micro- to centimetre scale) to the scale of large bends and deflections (1–100 s km), such as the Big Bend of the San Andreas fault.

The details of how different scale roughness or fault topography influences the dynamics of earthquakes and fault mechanics is not entirely understood. At the scale of laboratory experiments (millimetre to decimetre scale), the static coefficient of friction is suggested to be independent of roughness if normal stresses are high (Byerlee 1970). Nevertheless, small-scale roughness, that is, the roughness of planar, ground surfaces ranging from micrometres to millimetres influences the frictional properties of rock samples in many different ways. For example, the breakdown slip distance required for the coefficient of friction to drop during the initiation of slip depends on the initial surface roughness (e.g. Dieterich 1979; Okubo & Dieterich 1984). Consequently, larger roughness can increase the stability of motion along a fault in that it favours stress release through the creation of small-slip events instead of unstable slip events, that is, stick slips. This is supported by the observation of relatively high b-value (larger proportion of small-seismic events) of acoustic emission (AE) events on rough compared to smooth faults (Sammonds & Ohnaka 1998). Besides the influence on seismic event size distributions, roughness also influences the stress drop of slip events at laboratory scale (Okubo & Dieterich 1984) and at the scale of natural faults (Candela *et al.* 2011a). Similarly, the distribution of slip on faults is related to roughness, assuming that local stress variations are connected to fault roughness (Candela *et al.* 2011b). A direct connection between local stress heterogeneity and fault roughness has been observed through mapping the size distributions of contacts on translucent material interfaces (Dieterich & Kilgore 1996). Rougher faults are associated with smaller effective contact area, and the stresses at individual asperities are higher, whereas smooth surfaces exhibit more contacts over which the loading stresses are distributed. Thus, in addition to the distribution of slip, roughness influences the distribution of stress and strength along faults. This is also the case in the presence of gouge for which roughness increases the amount of stress required to shear a gouge layer (e.g. Sammis & Steacy 1994; Rathbun *et al.* 2013).

The roughness of natural faults has been studied and mapped extensively for exhumed faults, revealing self-affinity of slip surfaces with similar roughness exponents and slip-related surface smoothing in direction of slip (e.g. Power *et al.* 1987; Sagy *et al.* 2007; Candela *et al.* 2009; Griffith *et al.* 2010; Candela *et al.* 2012). Faults with larger cumulative displacements are generally smoother in direction of slip than faults with small displacements (below 10–100 m) and appear polished at the smallest wavelengths (Sagy *et al.* 2007; Brodsky *et al.* 2011; Candela *et al.* 2012). Progressive fault smoothing is most likely caused by abrasional wear, which could be a mechanism for fault evolution (Brodsky *et al.* 2011). Sagy *et al.* (2007) pointed out that the fault smoothing process might be limited to the first ∼100 m of fault displacement after which fault roughness remains largely constant. Systematic changes in fault roughness due to slip may be associated with a tendency of faults to evolve into a state of less complexity and more localized slip (e.g. Chester *et al.* 1993; Ben-Zion & Sammis 2003; Rockwell & Ben-Zion 2007).

Fault evolution has also been documented as function of step overs per length scale and cumulative geological offset (Wesnousky 1988). Moreover, a decrease in the complexity of splay orientations may indicate that faults evolve to less geometric complexity (Wechsler *et al.* 2010). However, these geological observations are limited to fault traces or exhumed fault surfaces, thus providing little insight into 3-D fault topography and fault structure at seismogenic depths. At these depths, microseismicity provides the most readily available information about fault properties. A recent study highlighted a possible connection between fault structure and across-fault seismicity distributions in California (Powers & Jordan 2010). The authors suggested that fault smoothing, inferred from off-fault seismicity distributions, is active even at large fault displacements, that is, for faults that exhibit cumulative offsets of 5–315 km. In their study, Powers & Jordan use a connection between fault roughness and off-fault seismicity distributions described theoretically by Dieterich & Smith (2009). The latter investigated stress interactions and sliding characteristics of simulated 2-D faults with random, fractal roughness in a purely elastic medium. The introduction of fault roughness and resulting geometric irregularities was associated with stress heterogeneity, including off-fault stresses. These off-fault stresses depended strongly on the fractal character of the fault geometry. The off-fault stress relaxation rates, $\dot{S}_{\mathrm{R}}$, were predicted to decrease as a power law with distance from the fault, y:

$$\dot{S}_{\mathrm{R}} = kG\beta y^{-(2-H)}, \tag{1}$$

where G is the shear modulus, β is a pre-factor that controls the total power of the spectrum, k is a constant that depends on fault slip rate and H is the Hurst exponent which describes the fractal roughness. In the brittle seismogenic crust, off-fault stresses are likely released in form of secondary cracks within the fault's damage zone. Consequently, the resulting seismicity distribution follows a power law with an exponent that is linearly related to fault roughness assuming that the surfaces are in contact everywhere. This has been tested for faults in California, confirming a general power-law decay of near-fault seismicity (Hauksson 2010; Powers & Jordan 2010). Furthermore, Powers & Jordan (2010) quantify the linear relation between off-fault seismicity exponent and fault roughness assuming that the 2-D fault roughness model can be applied to strike-slip faults. They obtain

$$\gamma = 2 - H, \tag{2}$$

where γ is the power-law exponent of seismicity decay with fault-normal distance.

To test this hypothesis, we performed frictional sliding experiments on planar fault surfaces with pre-defined roughness. Previous studies on natural seismicity (Hauksson 2010; Powers & Jordan 2010) could not establish a direct connection between seismicity and roughness because fault roughness can only be assessed for exhumed faults whereas seismicity typically occurs at several kilometres depths. Our experiments enable us to investigate both roughness and seismic off-fault activity in form of AE events under seismogenic conditions. AEs have proven to be effective in documenting both fault structure and stresses in a range of experiments. Spatial variations in the statistics of AE events during earthquake analog experiments were observed to be connected to along-strike fault structural heterogeneity and asperity locations (Goebel *et al.* 2012). Moreover, AE analysis can provide vital insights into the stress variations during macroscopic failure of rock samples (e.g. Scholz 1968; Main *et al.* 1992; Goebel *et al.* 2013b) and microfailure of asperities (McLaskey & Glaser 2011). AE studies also highlight similarities between the statistics of natural seismicity and AE events during rock-failure and stick-slip sliding (e.g. Scholz 1968; Goebel *et al.* 2013a; Vallianatos *et al.* 2013). The frequency–magnitude distributions of AE events can be described, for example, by non-extensive statistical physics, further emphasizing the non-linearity of the faulting process in both laboratory and nature as well as the importance of long range interactions prior to large failure events (Tsallis & Brigatti 2004; Vallianatos *et al.* 2012).

In the following, we scrutinize the existence of off-fault microcracking through AE event and thin-section analysis. We then investigate the characteristics of the off-fault activity distribution, including a detailed test for power-law behaviour. This is followed by a study of controlling parameters on off-fault activity, namely, variations in roughness and normal stress. Finally, we discuss our findings with regard to the understanding of natural seismicity variations.

2 EXPERIMENTAL DATA AND METHOD

We report on five frictional sliding experiments on homogeneous, isotropic Westerly granite samples. Westerly granite exhibits varying grain sizes between 0.05 and 2.2 mm with an average grain size of 0.75 mm (Byerlee & Brace 1968; Stesky 1978). The employed cylindrical (height = 100 mm, radius = 25 mm) samples were prepared with saw-cuts at a 30° angle to the loading axis (Fig. 1). The resulting surfaces were ground using different grain size

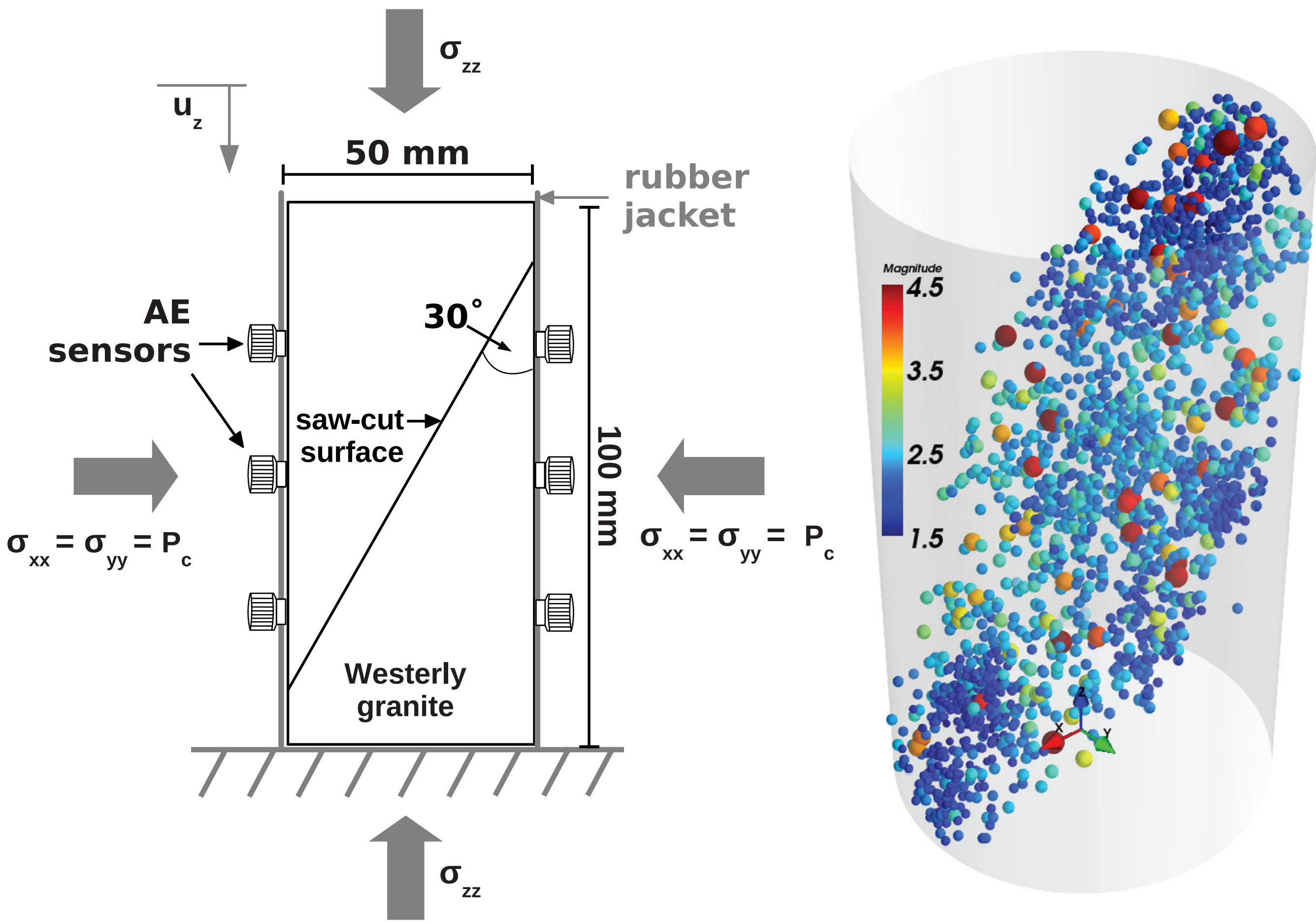

Figure 1. Sample geometry and loading conditions for saw-cut faults with different initial surface preparation (left-hand side). AE hypocentre locations highlight orientation of the fault at a 30° angle to the loading axis. Marker colours correspond to relative AE magnitudes estimated on a transducer-specific scale.

silicon-carbit abrasives. An overview of abrasive sizes, loading conditions, resulting stresses and displacements can be found in Table 1. All experiments were conducted at a constant axial displacement rate of 20 μm min^{-1} ($\dot{\epsilon} \sim 3 \times 10^{-6}$ s^{-1}). Within this work, we strove to investigate the influence of different fault properties on AE distributions in isolation. To this end, we conducted two sets of experiments: the first set at constant confining pressure to test the influence of different initial roughness (experiments: LR1-LP, HR2-LP and HR1-LP, where LR and HR denote low and high roughness and LP low pressure), and the other set (experiments: HR1-HP, HR1-IP and HR1-LP, where HP, IP and LP denote high, intermediate and low pressure) with the same initial surface finish to test the influence of different confining pressures and connected fault stress level.

We imaged the initial surfaces for each choice of abrasive using a White Light Interferometer (Zygo7300). Interferometry imaging is based on the interference pattern of a reference green light beam with a beam that reflects off a rough surface. By vertical movement of the sample and simultaneous image capturing, the interference, intensity envelope, and thereby the relative height of the imaged surface at each pixel is determined. A vertical resolution down to 0.1 nm was estimated by scanning a flat, reference surface (Silicon Carbide) with an estimated roughness of ∼6 order of magnitudes below the roughness of the initial surfaces used in our experiments.

We computed two different measures of initial surface roughness: The first measure was the rms (R_{rms}) which provides an estimate of the deviation from an average roughness profile

$$R_{\mathrm{rms}} = \sqrt{\frac{1}{n}\sum_{i=1}^{n}[p(z_i) - \bar{p}]^2}, \tag{3}$$

Table 1. Stress state, displacements and surface preparation of all experiments. σ_n, normal stress; τ, shear stress; μ, coefficient of friction; P_c, confining pressure; $U_{\max}$, maximum vertical displacement, mesh size and abrasive grain size describe the silicon carbit powder used to grind the inclined saw-cut surfaces.

Sample	σ_n (MPa)	τ (MPa)	μ	P_c (MPa)	$U_{\max}$ (mm)	Mesh size	Abrasive grain size (μm)
LR1-LP	221 ± 4	175 ± 4	0.79	120 ± 0.5	4.76 ± 0.003	F290	16.5–59
HR2-LP	222 ± 4	177 ± 4	0.79	120 ± 0.5	3.32 ± 0.003	F80	150–212
HR1-LP	178 ± 4	101 ± 4	0.57	120 ± 0.5	1.02 ± 0.003	F60	212–300
HR1-IP	225 ± 4	160 ± 4	0.71	133 ± 0.5	5.03 ± 0.003	F60	212–300
HR1-HP	244 ± 4	162 ± 4	0.67	150 ± 0.5	2.25 ± 0.003	F60	212–300

where $p(z)$ is the roughness profile. The other measure of roughness was computed from the power-spectral density of Fourier-transformed, roughness profiles, which were stacked for individual scans. This method provides an estimate of roughness as function of wavelength. Straight parts of the log-transformed power-spectra indicate self-affine scaling of wavelength and power. This can be quantified by computing the Hurst exponent (H)

$$P(\lambda) = \beta\lambda^{1+2H}, \tag{4}$$

where $P(\lambda)$ is the power at wavelength λ and β is a pre-factor that is related to the absolute vertical topography (Feder 1988; Amitrano & Schmittbuhl 2002; Candela *et al.* 2009). The Hurst exponent itself shows the distribution of power over different wavelength, that is, the relative power at small compared to large wavelengths. Instead of the Hurst exponent, one can express this relationship also by the roughness exponent α (e.g. Power & Durham 1997) which is linearly related to H (e.g. $\alpha = 1 + 2H$ for power spectral slopes) (e.g. Feder 1988). The Hurst exponent commonly occupies values between 0 and 1. A Hurst exponent of unity ($\alpha = 3$) indicates self-similar roughness scaling, whereas values of H below unity are connected to self-affine surfaces. For natural faults, H commonly ranges between 0.6 and 0.8 but also shows anisotropic behaviour, that is, smaller Hurst exponents in direction of slip (e.g. Sagy *et al.* 2007; Candela *et al.* 2009, 2012; Renard *et al.* 2013).

Frictional sliding of the rough surfaces under high pressures resulted in large AE catalogues containing 1268–10 907 events. The AE events had an amplitude range of about 4 orders of magnitude. Events were located by traveltime inversion of automatically picked first P-wave arrivals. We used AE sensors both as receivers and active pulse senders. The latter was to estimate seismic velocity changes throughout the experiments to improve the AE location accuracy. Similarly to Lockner *et al.* (1991), we limited our analysis to high quality events, that is, AEs that were recorded at eight stations or more and a traveltime residual ≤ 0.5 µs. In general, the location uncertainty was estimated between 1 and 4 mm, depending on the extent of fault-induced velocity perturbations and the proximity of an event to the edge of the sample. Average uncertainties could be lower for certain regions and experiments, especially for simple geometries like saw-cut samples.

2.1 Across-fault activity profiles and power-law parameter estimates

To analyse spatial characteristics of AE catalogues for experiments with different roughness, we projected the recorded AE events into a fault-specific coordinate system and computed across fault activity profiles. The AE activity was generally symmetric with respect to the fault axis allowing for a stacking of AE events from both sides of the fault. We deployed two methods to quantify the distribution of events with distance to the slip surface. The first method follows previous studies of natural seismicity (Felzer & Brodsky 2006; Hauksson 2010; Powers & Jordan 2010). It is based on an estimate of the linear density of AEs (linear density distributions will be referred to as LDDs in the following) by sampling a constant number (N) of nearest neighbour events starting from the fault centre (Silverman 1986). We then determined the area covered by each sample from the distance of the Nth event and normalize by the total fault area and duration of the experiment. Changes in N mainly influence the smoothness, and distribution tail whereas the slope remains largely stable for large sample sizes.

We also computed cumulative distributions of AE events as function of distance to the slip surface. The advantage of this method is that it is not prone to binning artefacts. Moreover, cumulative distributions depict many details of the trends in the data especially towards the tail of the distribution. The LDDs, on the other hand, represent the data in a smoothed form which can be advantageous to diminish the influence of individual outliers. Furthermore, LDDs depict regions of constant AE density as horizontal trends in the data and power law cut-offs can be estimated from the deviation from linearity of the activity fall-off close to the fault centre. The slope below the power-law cut-off can be determined by least-squares fitting since every data point contains the same number of seismic events hence same statistical significance.

Due to the consistent curvature of cumulative distributions, it is more complicated to estimate the power-law cut-off. For this reason, we compute the minimum cut-offs for our data (Y_{min}) using the maximum Kolmogorov–Smirnoff distance (KS-distance) between the observed distribution and modelled power-law distribution at varying values of Y_{min} (Clauset *et al.* 2009). The best parameter estimates of Y_{min} and γ will minimize the KS-distance between model and observation. The maximum likelihood estimate (MLE) of the power-law exponent is given by (e.g. Newman 2005; Clauset *et al.* 2009):

$$\gamma = 1 + n\left(\sum_{i=1}^{n} \ln \frac{Y_i}{Y_{\mathrm{min}}}\right)^{-1}. \tag{5}$$

Here, Y_{min} is the minimum bound, γ is the power-law exponent, n is the number of data points above Y_{min} and Y_i are the observed distance values above Y_{min}. The MLE is independent of sampling and less sensitive to variations in the distribution's tail compared to least-square estimates of binned, log-transformed data (Clauset *et al.* 2009). For the MLE, we can estimate the goodness-of-fit using a Monte-Carlo resampling approach: We created synthetic data using the best-fitting power-law parameters, computed the corresponding KS-statistics and compared it to the KS-statistic of the observed data set (Clauset *et al.* 2009). The goodness-of-fit (p-value) is then simply the fraction of cases for which the synthetic KS-distances are larger than the empirical distance. Large p values [here we choose a value above 0.1 following Clauset *et al.* (2009)] suggest that a power-law distribution is a plausible hypothesis whereas small p values would require the rejection of the power-law hypothesis.

3 RESULTS

The triaxial loading of our five samples resulted in different deformation characteristics along the saw-cut surfaces. An overview of the total vertical displacements, initial surface treatment and the stress conditions on the faults can be found in Table 1. The normal stresses varied between 178 and 244 MPa for different experiments with the largest normal stress for experiment HR1-HP which also exhibited the largest confining pressure. The initial stress increase was predominantly linear for all experiments (Fig. 4c). This was followed by extended periods of non-linear stress increase accompanied by higher AE activity. Experiment LR1-LP produced three stick-slip events with shear stress drops in the range of ≈107–173 MPa. For this experiment, we determined the normal stress in Table 1 from the average, peak stress before the three stick-slip events. To ensure comparability, we only analysed AE events that occurred before the first stick-slip event and compared the corresponding AE distribution to the initial surface roughness. At the beginning, we will focus on experiments HR2-LP, HR1-LP and

LR1-LP, which were conducted at the same confining pressure (P_c = 120 MPa) but different surface finish. LR1-LP resembles a polished surface with no apparent topography whereas both HR2-LP and HR1-LP appeared rough during visual inspection before the experiments.

3.1 Initial surface roughness

We determined the initial roughness of the three different surface-finishes with mesh sizes F290, F80 and F60 (see also Table 1 for different experiments and corresponding mesh sizes). The power spectra of all surfaces exhibited several decades of self-affine scaling between wavelength and power (Fig. 2a). highlighting the fractal character of the roughness within that scale range. The smooth surface (F290) showed a characteristic roll-off and flattening of the spectrum above ∼0.1 mm. The rough surfaces started to deviate from linearity of the power spectra at larger wavelengths ($\lambda > 0.2$ mm). The flattening of power spectra at large wavelength is related to the planarity of the surfaces which introduces a maximum wavelength of roughness and a corresponding roll-off in power (Persson *et al.* 2005). Below the roll-off wavelength, F290 appears smoother (less power) at all wavelength than F80 and F60, and also above, F290 shows smaller power at the largest wavelengths. F80 and F60 exhibit very similar power spectra that only deviated at the largest wavelengths.

To understand the possible role of fractal roughness in controlling seismic off-fault activity, we are interested in changes in slopes of the power spectra. To this end, we computed the roughness exponents, α, for the fractal range of power spectra (Fig. 2b). F60 and F80 exhibited largely identical values of α = 1.92 and 1.93, respectively, whereas F290 exhibits a substantially smaller value of α = 1.57.

3.2 AE hypocentre locations, off-fault microcracks and loading curves

To test if seismic event distributions and off-fault activities are connected to different roughness, we analysed high precision AE catalogues. AE events generally highlight the orientation and extent of the saw-cut surfaces (Fig. 3). We scrutinized the quality of surface finish before and during the experiments. The latter was accomplished by comparing the extent of AE hypocentre locations with the faults' surface area, which was a good indicator for surface planarity and homogeneous surface contacts. Experiments with localized AE clustering, which is indicative of uneven surface finish resulting in partial loading of the surfaces, were not included in this study.

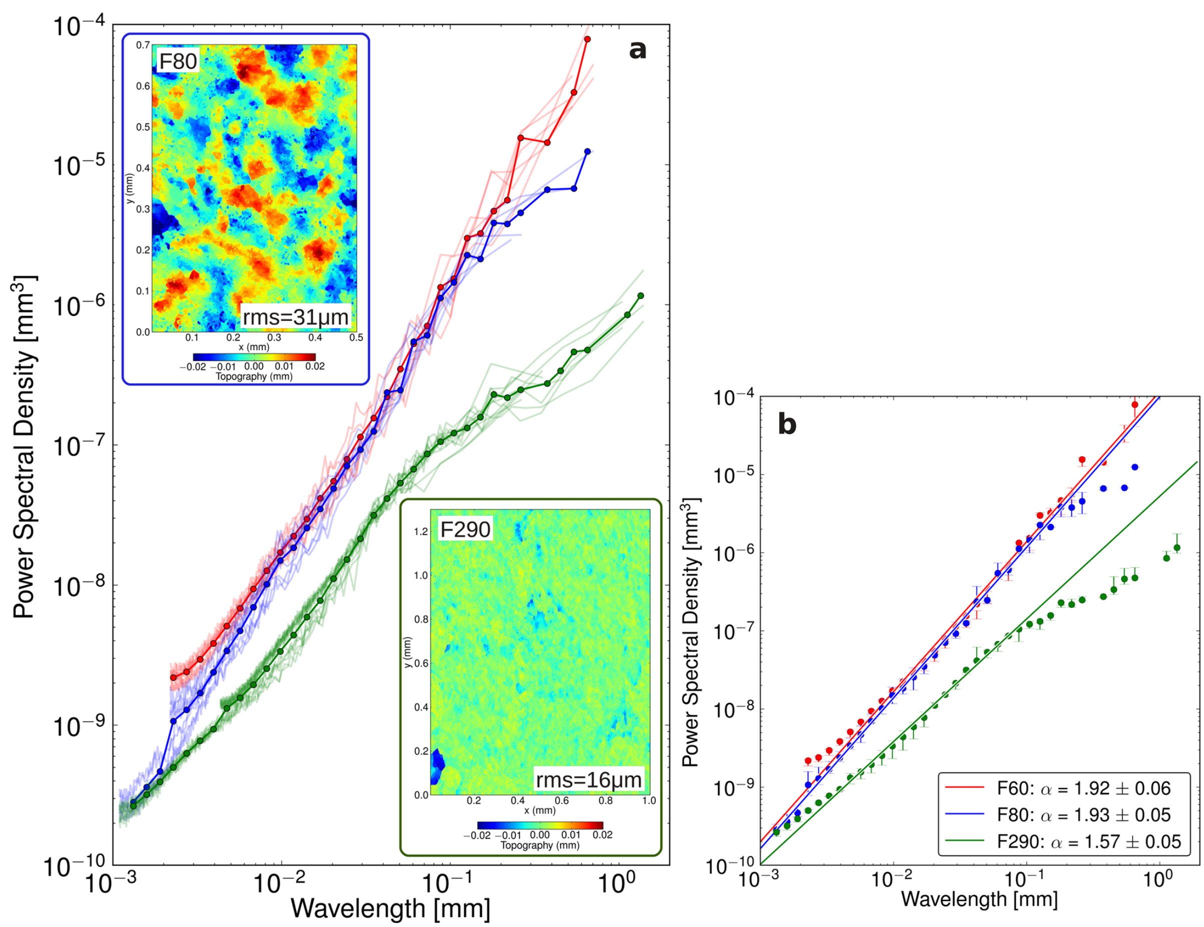

Figure 2. Power-spectral density as function of wavelength for smooth and rough faults. (a) Stacked power spectra for different roughens profiles of surface F290, F80 and F60 (see legend in b). The surface IDs correspond to the mesh sizes in Table 1. The experiments were prepared in the following manner: F290 – LR1-LP, F80 – HR2-LP, F60 – HR1-HP, HR1-IP and HR1-LP. Upper and lower insets depict the topography within the initial roughness of a rough and a smooth surface. (b) Least-square fits of average power-spectral density of all scans of the individual surfaces. F80 and F60 have comparable roughness exponents whereas F290 has a substantially smaller exponent.

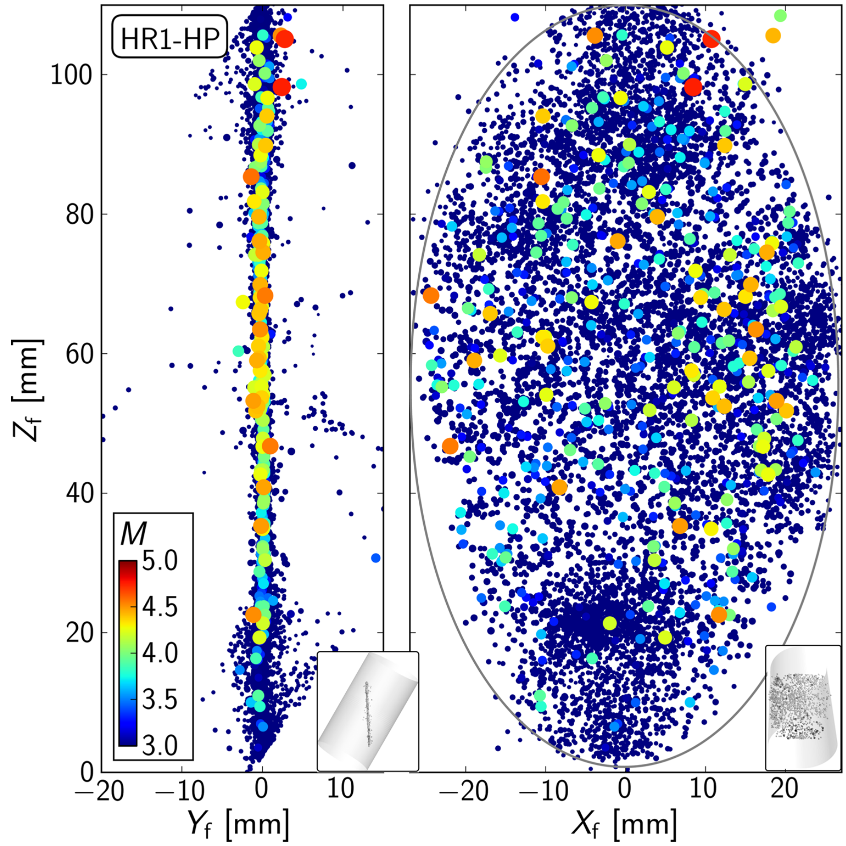

Figure 3. AE hypocentre locations of experiment HR1-HP, projected into the fault coordinate system and viewed in a plane perpendicular (left-hand side) and parallel (right-hand side) to the saw-cut surface. Marker colours correspond to AE magnitudes on a scale that is specific to the present experimental set-up.

Fig. 3(left-hand side) highlights the orientation and extent of the AE event populations of experiment HR1-HP. AEs occurred in a narrow zone of a few millimetre width around the fault axis. Large magnitude events predominantly occurred on the fault plane whereas smaller magnitude events were located at maximum fault-normal distances of $Y_\mathrm{f} = 10$–20 mm from the fault plane, thus suggesting pervasive microcracking away from the fault.

We test the existence of off-fault microcracks through inspection of post-experimental thin sections and histograms of the AE activity with increasing Y_f. The thin-section images revealed a network of cracks and connected pore-space that extended out to a fault-normal distance of ∼10 mm (Fig. 4a). Similarly, the largest AE activity was observed within the first 5–10 mm (Fig. 4b). Within this range of fault-normal distances, the AE activity decreased rapidly until it reached an approximately constant rate for $Y_\mathrm{f} > 10$ mm. Thus, both AE event distributions and thin sections provide evidence for the existence of seismically active microcracks at distances up to ∼18 mm from the fault axis.

3.3 Across-fault activity profiles and power-law exponent estimate

In the following, we will compare the two aforementioned methods to quantify off-fault activity distributions. We start by computing LDDs using constant AE sample sizes of $N = 20$ events (Fig. 5a). Expectedly, this method depicts a plateau in the AE activity close to the fault axis at distances of $Y_\mathrm{f} \lesssim 0.4$–$0.7$ mm. This is followed by a rapid decrease in AE density at larger distances. We estimated the slope of this decrease (γ) using a least-squares fit. The power-law exponents are similar for the two rough surfaces (HR2-LP: $\gamma = 2.63 \pm 0.17$, HR1-LP: $\gamma = 2.52 \pm 0.42$) whereas the smooth surface (LR1-LP) exhibits a substantially higher exponent of $\gamma = 3.5$. To test the stability of these results, we compute the power-law exponent using the MLE (eq. 5). The MLE power-law fit and cumulative distribution of each of the three experiments is shown in Fig. 5(b). The minimum cut-off values Y_min were computed by minimizing the KS-distance between observed and modelled distributions. These values were also used to define the resolution limit of both cumulative and AE density distributions. For details about the role of Y_min and its connection to hypocentral uncertainties, see Section 3.4. The power-law exponent increases for the different experiments from $\gamma = 2.57$ for HR2-LP to $\gamma = 2.74$ for HR1-LP and lastly to $\gamma = 3.11$ for experiment LR1-LP. In comparing the least squares and MLEs, we notice an apparent difference for the experiments with relatively small sample sizes (HR1-LP, LR1-LP) while HR2-LP exhibits largely constant exponents. The discrepancy is likely due to a combination of binning artefacts in the LDDs and large uncertainties of least-squares fit for small sample sizes. The latter can result is insufficient data spread for a reliable least-square fit of LDDs. For example, the data points of experiment HR1-LP are concentrated between 0.7 and 2 mm, providing a small range for a least-square fit and a relatively large error of 0.42. Small changes in the furthest data points can thus influence the power-law exponent substantially. The MLE, on the other hand, is insensitive to binning artefacts and outliers in a distribution's tail (Clauset *et al.* 2009).

To further investigate the relative differences in the observed distributions, we computed the power-law exponent as function of increasing values of Y_min between 0.1 and 3 mm (Fig. 6). We expect γ to increase rapidly when approaching the true Y_min value from

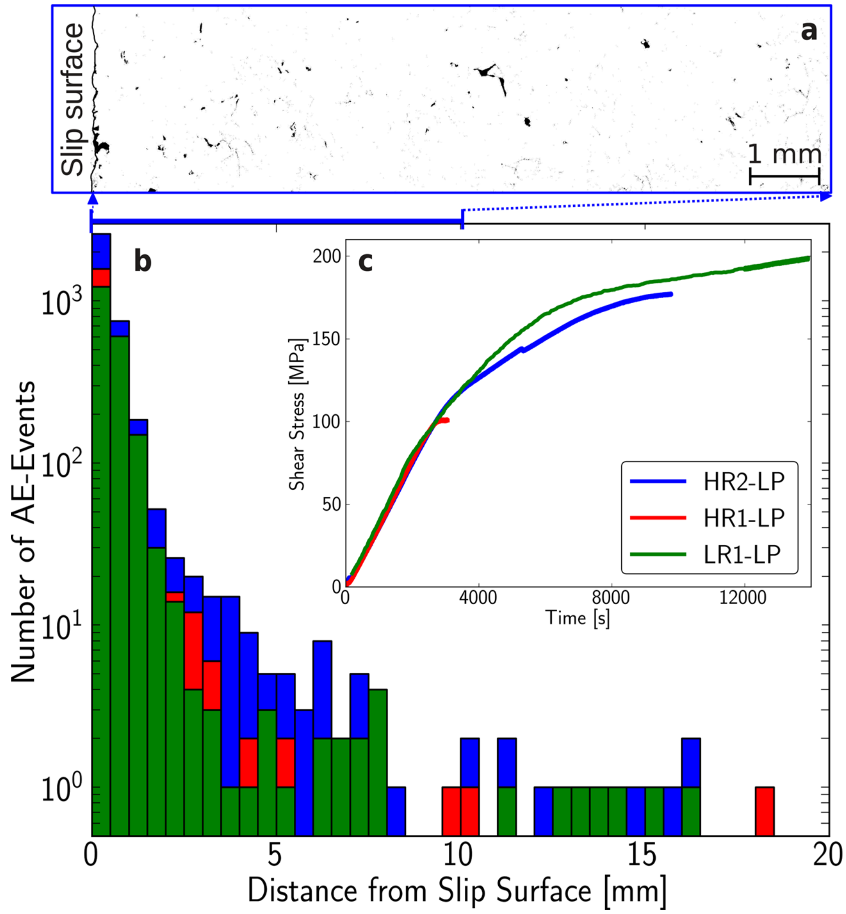

Figure 4. (a) Post-experimental microcrack distribution in a fault-perpendicular thin section. Here, we only show the relevant microcracks which appear as black, linear features in a thin section. (b) Seismic activity histograms as function of distance from the slip surface for three surfaces with different initial roughness (see legend or Table 1 for mesh sizes used for surface grinding). All surfaces show clear evidence of seismic activity away from the slip surface. This activity decayed the fastest for the smooth surface and slower for the rougher surfaces. (c) Changes in fault shear-stress during loading of the three different, rough surfaces.

below and to stay roughly constant above, over the range where the power-law holds. This behaviour could be observed for experiment HR1-LP which approached a value of $\gamma \sim 2.7$ for $Y_{\min} > 0.5$, and is in agreement with the predominantly linear trend of the cumulative distribution on logarithmic scales (Fig. 5b). The other two experiments exhibited trends in γ that are stable over shorter ranges (i.e. 0.7–1 for LR1-LP and 0.5–1 for HR2-LP). The combination of stability of γ and statistical error give an estimate for possible range of $Y_{\min}$. Above $Y_{\min} = 1.5$, the uncertainty in γ becomes too large, providing an upper bound for $Y_{\min}$. Consequently, one can determine, that within the possible range of $Y_{\min}$, LR1-LP has the largest value of $\gamma \approx 3$–3.1 while HR1-LP shows lower values ($\gamma \approx 2.6$–2.75) and HR2-LP consistently shows the lowest values ($\gamma \approx 2.3$–2.55).

3.4 Testing the power-law hypothesis

We tested if the observed distributions can be described by a different model, for example, a simple summation of normal distributions which represent Gaussian-uncertainties in hypocentre locations. To this end, we created random uniformly-distributed hypocentre locations within a fault zone with varying widths, $w = 0.1$–5.1. Instead of discrete event locations, we prescribed each hypocentre a random Gaussian uncertainty with varying width (Fig. 7a) and computed the cumulative distributions and power-law exponents for the resulting synthetic distributions (Fig. 7b). As a reference, we also plotted the cumulative distribution and γ as function of $Y_{\min}$ for one of the observations (HR1-HP). The synthetic Gaussian distributions generally overpredict the number AE events close to the slip surface while decaying too rapidly at larger distance thus providing a poor fit to the observation. The corresponding estimates of γ express the continuous curvature of the synthetic distributions, that is, they never show the plateau of constant exponents characteristic for power-law behaviour. Thus, hypocentral uncertainties alone cannot explain the observed across-fault activity profiles.

After ruling out that the observed distributions are simply caused by Gaussian errors, we tested the hypothesis that the observed distributions are a convolution of hypocentral uncertainties and a power-law distribution. To this end, we randomly sampled fault-normal distances from power-law distributions with the empirically determined exponents. We then assigned a value of Gaussian uncertainty to each distance value and computed the resulting cumulative distribution and power-law exponent (Fig. 8). The resulting distributions mimic the characteristics of the observed distribution including the region of high AE density close to the fault axis, a gradual roll-off zone and transition into a power-law dominated distribution at increasing fault-normal distances. The convolution of power-law and Gaussian uncertainties changes the parameter estimates of an initial power law in two different ways: First, it generally leads to a slight overestimate of the power-law exponent due to the faster

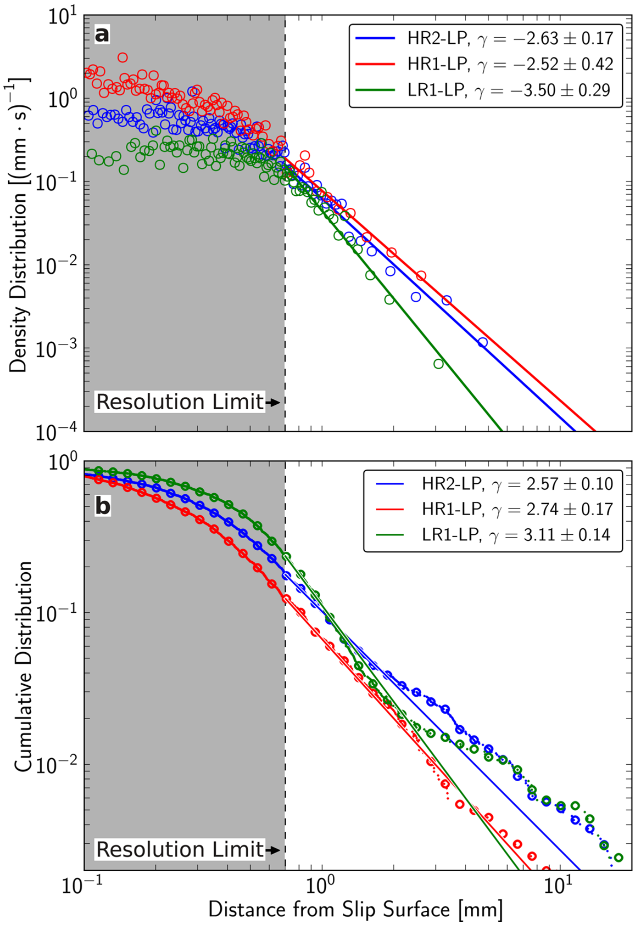

Figure 5. (a) AE density distribution as function of fault-normal distance, estimated by LDDs. The corresponding power-law exponents for each experiment are shown in the legend on the upper right. The shaded, grey area depicts the lower resolution limit of across fault activity profiles which is defined by the lower bound of the power law as discussed in the text. (b) Cumulative distributions of seismic activity as function of fault-normal distance and MLE of corresponding power-law exponents. The distributions are depicted for log-bins between 0.1 and 20 mm and exponents are computed for activity above minimum cut-off.

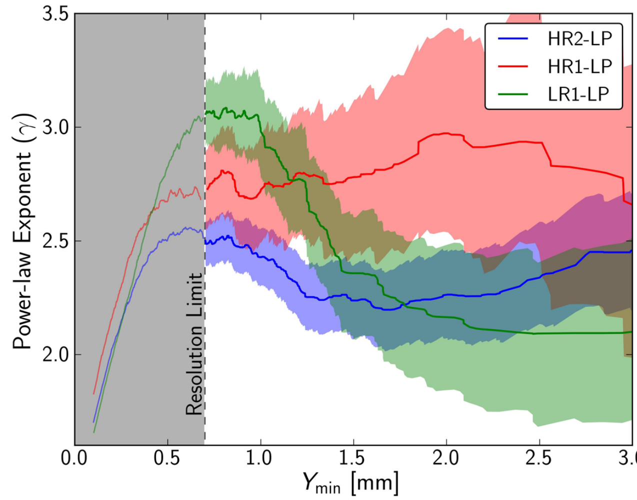

Figure 6. Changes in power-law exponent α as function of minimum cut-off $Y_{\min}$. The stability of α above the estimated minimum cut-off ($Y_{\min} = 0.7$) is a good indication about the range of the power-law behaviour.

decay of Gaussian distributions at intermediate distances. This is most pronounced for large power-law exponents. Second, large normal distribution widths systematically increase the roll-off zone and connected minimum cut-offs of the initial power law. Nevertheless, the depicted distributions highlight that the observed data could be modelled by convolving power law with normal distributions. Fig. 8 shows the best-fitting (minimum KS-distance) distribution exemplified for experiment HR2-LP which has a Gaussian-width of $\sigma \approx 2$ mm.

We systematically tested the connection between the observed parameter estimates $Y_{\min}$, γ and the parameters of the synthetic distributions γ^* and σ, where γ^* is the exponent of the initial power law and σ is the width the normal distribution. The latter gives an estimate of the expected hypocentral uncertainty. We simulated a range of distributions with increasing Gaussian widths and estimated the minimum cut-offs ($Y_{\min}$) using the minimum KS-distance between synthetic and modelled distribution (Fig. 9b). Following this method, the theoretical prediction of the Gaussian uncertainty for a power law with lower cut-off $Y_{\min} = 0.7$ convolved with a normal distribution is $\sigma = 1.4$–2 mm depending on the power-law exponent. These values are in approximate agreement with AE location errors ($\sigma \approx 1.7$ mm) estimated for known sensor locations that were used as active sources.

Assuming that the width of the Gaussian remains constant for all experiments, which is supported by constant array sensitivity, we could also test the influence of the normal distribution on the observed power-law exponents (Fig. 9a). As previously noted, the observed power-law exponent (γ) was slightly higher than the true power-law exponent (γ^*) due to the presence of Gaussian uncertainty. The computed synthetic distributions suggest an approximately linear relationship between γ and γ^*, enabling a simple correction of the observed exponents. This correction is slightly larger for higher exponents whereas small exponents are less influenced by the Gaussian uncertainty and consequently deviate less from the true value. In the following, we will use the value of the power-law exponent corrected for Gaussian uncertainty of hypocentre locations (see Table 2 for both γ and γ^*).

We estimated the goodness-of-fit for the observed power-law exponent resulting in p-values between 0.11 and 0.64. This supports that a power law is a valid hypothesis for the observed distributions since none of the power-law fits can be rejected at the chosen confidence level. The computed p-values are related to the extent of the power law, which is seen at both the degree of linearity of cumulative distributions (Fig. 5) and the stability of γ-values as function of $Y_{\min}$ (Fig. 6). For example, experiment HR2-LP depicts a comparably low p-value (0.11) and corresponding larger fluctuations in γ as function of $Y_{\min}$, whereas HR1-LP showed a higher p-value (0.64) and stable values of γ above $Y_{\min}$. The computed p-values are somewhat sensitive to the number of samples within the observed distributions especially in case of very small sample sizes which can lead to an unrealistic inflation of p-values (Clauset *et al.* 2009). A combination of the here proposed measures can largely prevent miss-interpretations of p-values, and should generally be applied to seismicity fall-off studies.

3.5 Roughness and off-fault AE distributions

We now test the initial hypothesis that seismic off-fault activity is connected to the fractal roughness of a slip surface. Fig. 10 shows the off-fault activity exponents as function of Hurst exponent. The

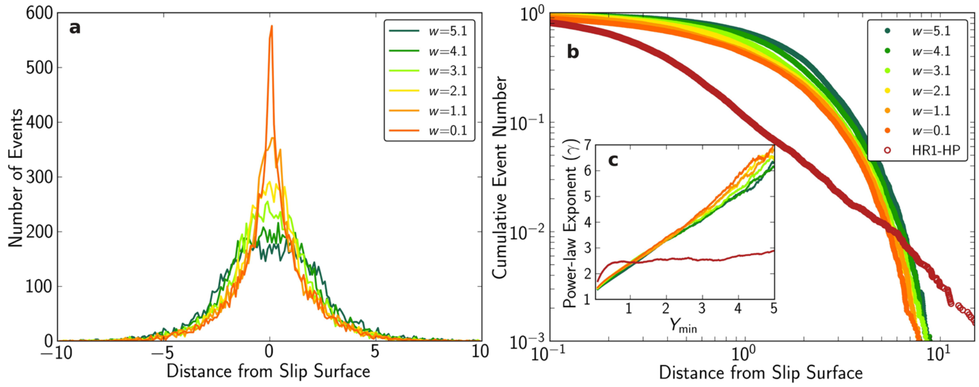

Figure 7. (a) Simulated Gaussian distributions for different fault widths (w) see text for details. (b) Cumulative, synthetic Gaussian distributions for different fault widths (coloured markers) and power-law distribution with exponent and minimum cut-off that resemble the observed values. The inset (c) displays differences in exponent as function of minimum cut-off assuming a power-law model for the data. The red line shows observed values of γ as function of $Y_{\rm min}$ for experiment HR1-HP, highlighting that the Gaussian distributions are a poor description of our data.

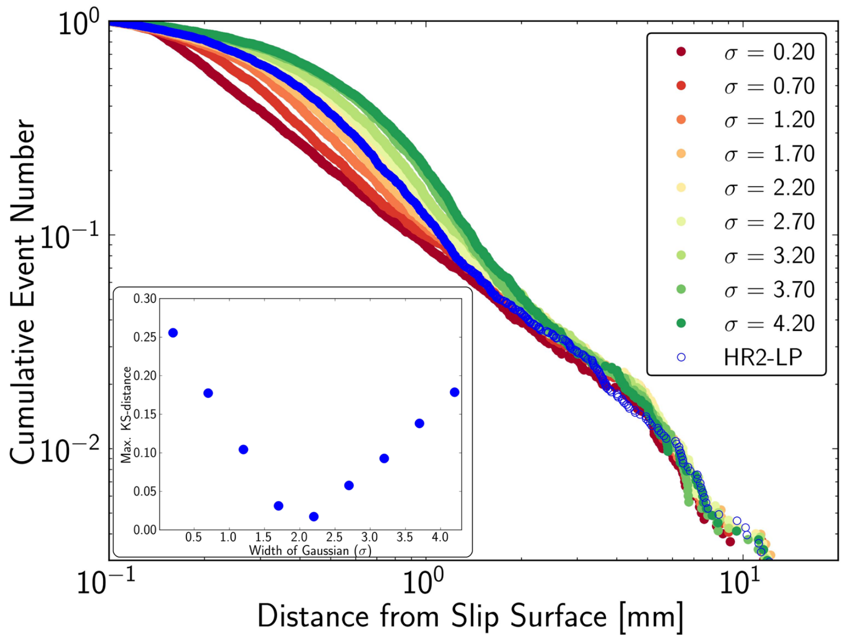

Figure 8. Observed (blue circles) and synthetic distributions (coloured markers) computed from power laws with Gaussian uncertainty. The best-fitting synthetic distribution was estimated by minimizing the KS-distance between the different distributions (inset).

smooth fault is connected to a higher γ value while the Hurst exponent is substantially lower, which is in agreement with the hypothesis. The two rough surfaces, which exhibited a similar value of H, showed slightly different values of γ but both were substantially lower than the value for the smooth surface. The model in Dieterich & Smith (2009) suggests that the Hurst exponent should be linearly related to the off-fault activity exponent, γ in 2-D (eq. 1). We included this relationship in Fig. 10. Our results support a similar linear relationship, however, with a different regression intercept. Thus, a relationship of the form: $\gamma = 3 - H$ describes our data better. This discrepancy is likely due to the difference in geometric dimensions between model and laboratory fault zones, which results in a variation of the spatial extent of stress perturbations (see Section 4 for details).

3.6 Normal stress and off-fault AE distributions

Considering the difference in off-fault activity exponents between HR2-LP ($\gamma = 2.56$) and HR1-LP ($\gamma = 2.74$) at similar initial roughness, other mechanisms appear to influence γ as well. In the context of the current experimental series, a variation in fault stresses is a likely candidate that may change the off-fault activity. We investigated the influence of different normal stresses by conducting three experiments with the same initial roughness ($\alpha = 1.92$) but different confining pressures. Starting with experiment HR1-LP ($P_{\rm c} = 120$ MPa), we increased the confining pressure to $P_{\rm c} = 133$ MPa for experiment HR1-IP, and $P_{\rm c} = 150$ MPa for experiment HR1-HP. The power-law exponent of the off-fault activity changed with increasing confining pressures from 2.74 to 2.55 and 2.48 (Fig. 11). The respective goodness-of-fit values (p-values) can be found in Table 2.

The power-law exponents decrease in an approximately linear fashion with increasing normal stresses (Fig. 12). This indicates that faults under higher normal stresses can appear 'seismically rougher', in the sense that relatively more of the seismic activity is located at larger distances from the slip surfaces (see inset in Fig. 11), and the off-fault activity exponents become smaller. The rate of change in γ due to the observed range of normal stress

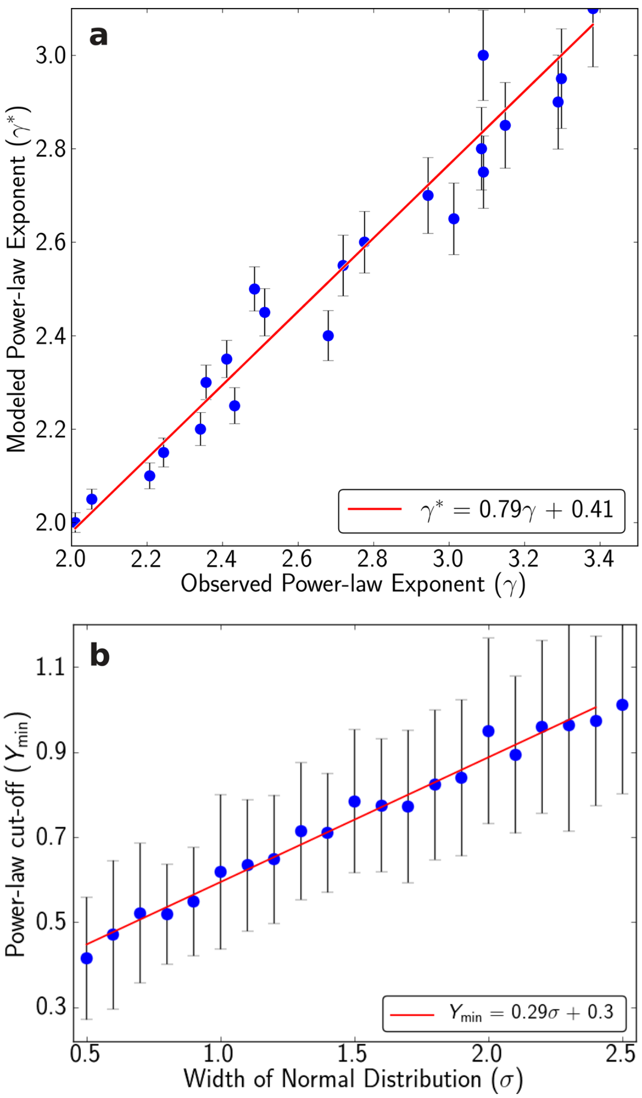

Figure 9. Changes in power-law parameters due to the presence of Gaussian uncertainty. (a) Connection between true (γ^*) and observed (γ) power-law exponent assuming constant Y_{min} and σ. (b) Influence of σ on Y_{min}. For our experiments a value of $Y_{\mathrm{min}} = 0.7$ suggests a hypocentral uncertainty between 1.4 and 2.0 mm.

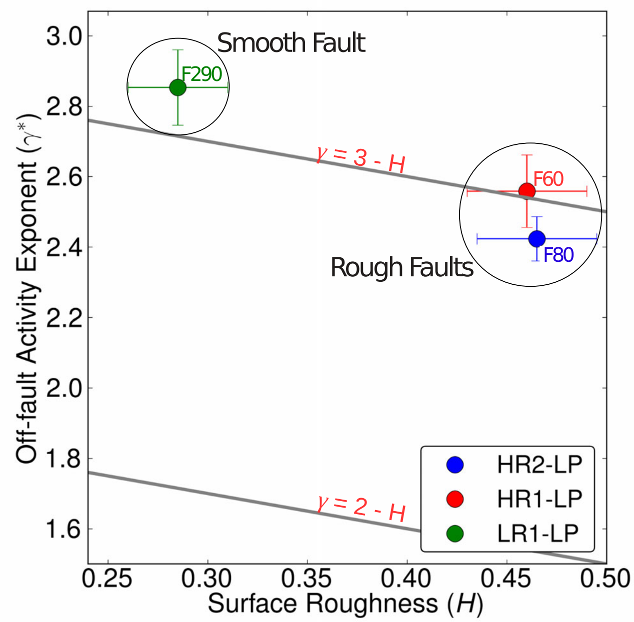

Figure 10. Increasing surface roughness results in decreasing off-fault activity exponents. Rough faults (HR2-LP and HR1-LP) are highlighted by a dark circle to the right and the smooth fault (LR1-LP) is located at the upper left. The labels next to the markers correspond to the abrasive mesh size used for initial surface preparation. Grey lines show the theoretical prediction of a connection between roughness and off-fault activity. The corresponding equations are depicted above the grey lines.

increase ($\sim 4 \times 10^{-3}$ MPa) can also account for the difference in γ between HR2-LP and HR1-LP ($\Delta\gamma \sim 0.18$) due to a change in normal stress of $\Delta\sigma_{\mathrm{n}} = 44$ MPa. These considerations are under the assumption of a simple linear relationship between increasing normal stresses and γ. More complex interactions between fault roughness and stress state may also result in a more complex relationship between these quantities and the off-fault activity exponents (see Section 4).

4 DISCUSSION

4.1 Influence of roughness on seismic off-fault activity

Our results are in agreement with theoretical predictions of a connection between surface roughness and the rate of stress relaxation with increasing fault-normal distance (Dieterich & Smith 2009). While these stresses could not be measured directly, the observed AE event distributions and post-experimental thin sections (Fig. 4a) are a good indicator for a stress release in form of brittle microcracking and associated seismic energy release. Fault roughness and connected geometric interaction at irregularities are likely involved in the creation of pervasive off-fault damage out to distances of ~10–20 mm. This process can, in addition to dynamic ruptures, play an important role in the creation of damage zones in the vicinity of natural faults (Dieterich & Smith 2009). Laboratory experiments (e.g. Zang *et al.* 2000; Janssen *et al.* 2001) and geological

Table 2. Results of off-fault activity and roughness analysis for all experiments. γ, observed off-fault activity exponent; γ^*, off-fault activity exponent corrected for Gaussian uncertainty; p-value, goodness-of-fit; α, roughness exponent; N_{AE}, total number of observed AE events; N_{AE}/s, AE-rate per second.

Sample	γ	γ^*	p-Value	α	N_{AE}	N_{AE}/s
LR1-LP	3.11 ± 0.15	2.85 ± 0.15	0.14	1.57 ± 0.05	1978	0.14
HR2-LP	2.56 ± 0.10	2.42 ± 0.10	0.11	1.93 ± 0.05	3787	0.33
HR1-LP	2.74 ± 0.17	2.56 ± 0.17	0.64	1.92 ± 0.06	2073	0.67
HR1-IP	2.55 ± 0.12	2.42 ± 0.12	0.36	1.92 ± 0.06	1268	0.01
HR1-HP	2.48 ± 0.06	2.36 ± 0.06	0.53	1.92 ± 0.06	10907	1.63

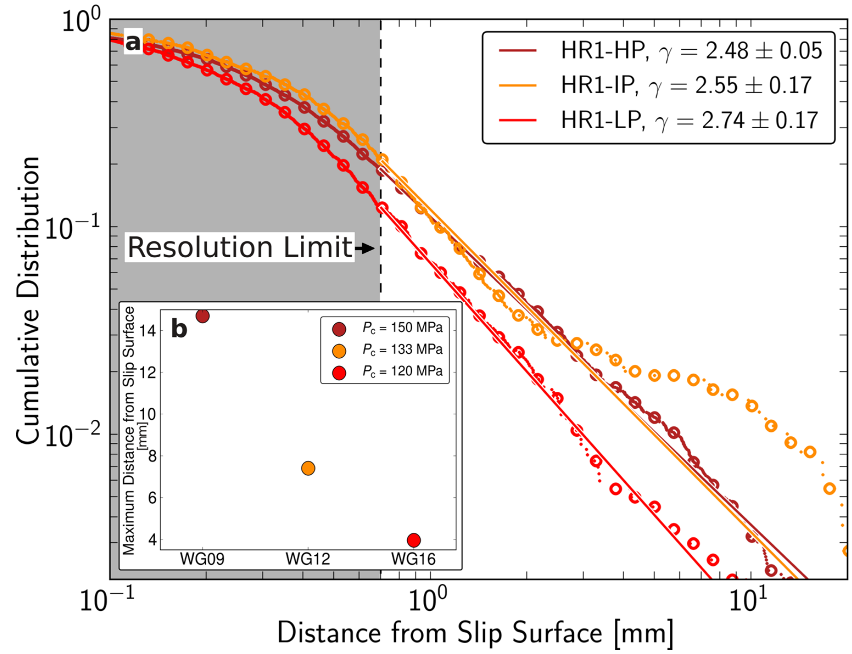

Figure 11. Influence of confining pressure on seismic off-fault distribution and maximum AE event distance from the fault axis (a) Cumulative distribution of AE events as function of distance from the slip surface for three experiments with different confining pressure (HR1-LP: $P_c = 120$ MPa, HR1-IP: $P_c = 133$ MPa, HR1-HP: $P_c = 150$ MPa) but same initial roughness. (b) Maximum distance of the furthest off-fault events. Here, we used the average distance of the furthest 50 AE events in millimetre to diminish the influence of individual outliers.

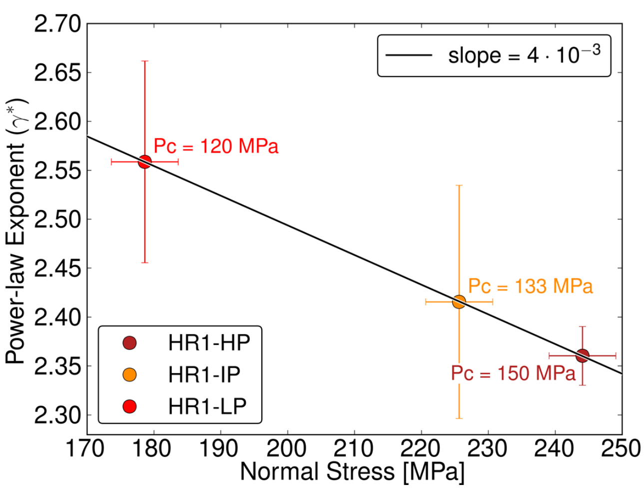

Figure 12. Increasing normal stresses lead to a decease in the off-fault activity exponent (γ). The three markers correspond to three experiments conducted at different confining pressures.

observations of natural faults indicate that fault wall-damage zones show crack densities that decrease exponentially, or as a power law, with distance from the fault (e.g. Anders & Wiltschko 1994; Mitchell & Faulkner 2009; Savage & Brodsky 2011). This type of damage is likely related to high strain at a propagating rupture tip and deformation around the fault as slip increases (e.g. Kim *et al.* 2004; Griffith *et al.* 2009; Xu & Ben-Zion 2013). The here discussed off-fault damage would predominantly be created during interseismic periods on rough faults and background stresses close to the critical stress. Within the scope of the current experimental series, we did not observe a systematic connection between the maximum range of the off-fault power law and the outer length-scale of the fractal fault geometry, as hypothesized by Dieterich & Smith (2009). This may be due to limited ranges of wavelengths over which the roughness of our surfaces can be considered as fractal. Moreover, the AE events at the farthest distance from the fault axis are likely associated with small-scale sample heterogeneities that radiate seismic energy at locally high stresses. This is especially visible for smooth faults with comparably localized AE activity, for example, LR1-LP which produced AE activity that was higher than predicted from a power law at large distances to the slip surface. For rougher faults, finite sample sizes may additionally influence the distribution at large distances ($Y_f \gtrsim 20$ mm).

We tested a proposed theoretical model that suggests a linear relation between fractal roughness and off-fault activity decay exponent, implying that rougher faults exhibit increased spatial extents of significant off-fault stresses (Dieterich & Smith 2009). This model and observations of actual seismicity led Powers & Jordan (2010) to posit that the relationship between off-fault activity exponent and fault roughness goes roughly as $\gamma = 2 - H$, where H is the Hurst exponent characterizing fault roughness. This scaling was based on the assumption that the 2-D approximation of Dieterich & Smith (2009) model holds approximately also in 3-D. Instead, our results suggest a scaling closer to the form $\gamma = 3 - H$ for fractally rough surfaces in 3-D, and this would also explain some of the larger off-fault activity exponents found in Powers & Jordan (2010). The faster decay of off-fault stresses with fault-normal distance in 3-D is consistent with the inference that stress should decay with distance (r) from asperities as $1/r^3$ in 3-D as opposed to $1/r^2$ in 2-D. Consequently, we use a more general form for the relationship between roughness and off-fault activity:

$$\gamma = c_g - H, \tag{6}$$

where c_g is the geometric dimension (see e.g. Mandelbrot 1982; Turcotte 1997).

4.2 Influence of normal stress and contact size distributions

In addition to the described influence of fault roughness, fault-normal stress was observed to change the decay rate of off-fault seismicity. Within the range of the here observed stresses, the normal stress showed an approximately linear relationship with γ, so that at higher stresses, a larger proportion of AEs occurred at increased fault-normal distances. Higher stress levels were also connected to an increase in the maximum distance of AEs (Y_{max}) from the fault axis.

The connection between roughness and fault stresses, and the resulting seismic event distributions is generally complex. Stress variations and the frequency-size distributions of seismic events have been investigated for fractally rough faults (Huang & Turcotte 1988). The authors computed random 2-D fractal surfaces to simulate combined stress-strength distributions on faults with different roughness exponents. They showed that the frequency-size distributions of seismic events follow a power law with an exponent (b-value) that is inversely proportional to the ambient stress level. Besides the correlation with stress, their model predicts a dependence of b-values on the fractal dimension of the initial stress-strength distributions.

Moreover, the normal stress distribution on a fault is strongly dependent on the amount and size of contacts. The scaling of these stress distributions (H_σ) is suggested to be related to the initial fractal roughness (H_{r}) over: $H_\sigma = H_{\mathrm{r}} - 1$ (Hansen *et al.* 2000), for surfaces that are perfectly mated. This relationship is strongly dependent on the ratio of effective contact area to total fault area so that the corresponding scaling of H_σ changes in a non self-similar fashion during contact area increases with larger normal stresses (Schmittbuhl *et al.* 2006). The here tested model (Dieterich & Smith 2009) does not account for the changes in the amount of effective surface area. Previous experiments on analog materials revealed that contact area increases with larger fault-normal stress and that the corresponding contact size distributions exhibit smaller scaling exponents for some materials, for example, acrylic and glass (Dieterich & Kilgore 1996). Lower scaling exponents are connected to an increase in the proportion of large contacts which is in agreement with our results, assuming a direct connection between the spatial extent of off-fault stress relaxation and on-fault asperity-size distributions. Consequently, the growth and coalescence of asperities is likely responsible for the observed changes in γ at increasing normal stresses.

Furthermore, the model in Dieterich & Smith (2009) does not account for possible size variations of seismic events that are connected to off-fault stress relaxation. A possible difference in AE sizes can influence both the off-fault activity exponent and the maximum extent of the distributions. This can be explored theoretically by linking event sizes to relative off-fault stress level assuming constant strength and experimentally by studying b-value variations as function of fault-normal distance. The latter requires very large AE catalogues, due to the power-law decay with distance from the slip surface which are not available within the scope of current experimental series.

For a more comprehensive understanding of underlying mechanisms of seismicity variations, a model that elucidates the influence of fractal roughness and stress changes on both off-fault activity and b-value is desirable.

4.3 Understanding off-fault density distributions of natural seismicity

The observed across-fault AE activity profiles show strong similarities to observations of natural seismicity (Fig. 13). In both cases, we observe an initial flat part of the distributions which is connected to constant AE density. The natural seismicity profiles are characterized by an inner (Y_{min}) and outer scale (Y_{max}), as well as a power-law fall-off that can be described by an exponent (γ). At large fault-normal distances ($Y > Y_{\mathrm{max}}$), one can observe a transition from power-law decay to the seismic background activity. The inner scale may indicate the half width of the inner fault zone or fault core (Powers & Jordan 2010). Our experiments highlight that the inner scale is also strongly influenced by hypocentral uncertainties which may lead to an inflation of the inferred fault zone width. The outer scale is not resolvable in our experiments due to limited sample dimensions. Our range of off-fault activity exponents (2.36–2.85) is within the upper range of those observed for Californian faults. The corresponding faults are considered mature faults with large cumulative offsets, comparably low complexity and increased smoothness. This indicates that mature faults can possibly be simulated in the laboratory by planar surfaces with little to no large-wavelength roughness. Young faults are suggested to have substantially lower values of γ indicating high fault complexity and roughness (Powers & Jordan 2010).

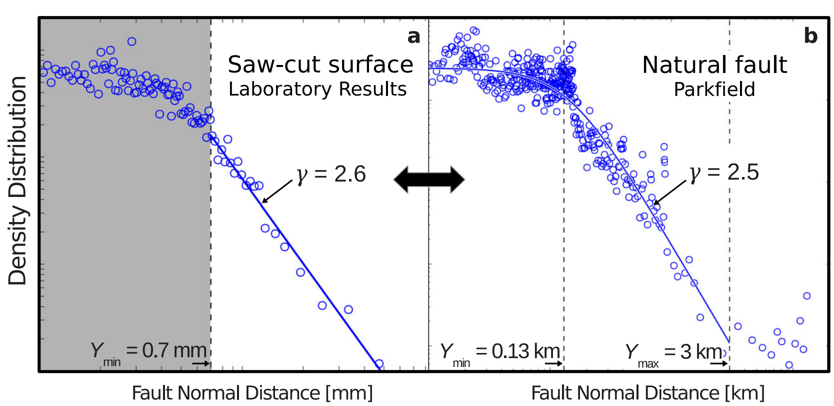

Figure 13. Off-fault activity profiles show similar characteristics in laboratory and nature. (a) AE event density as function of fault-normal distance for a planar fault with pre-defined roughness. Y_{min} is the minimum power-law cut-off which is controlled by the hypocentral uncertainty. (b) Seismic event density profile for the Parkfield section of the San Andreas fault (modified after Powers & Jordan 2010). Y_{min} is related to the half-width of the fault core. Y_{max} marks the transition to the background seismicity.

5 CONCLUSION

We conducted two sets of frictional sliding experiments on Westerly granite samples with pre-defined, initial roughness. The first set was conducted at constant confining pressure and different initial surface preparation revealing a correlation between surface roughness and seismic off-fault activity. Analogous to observations of natural seismicity, the seismic off-fault activity in our laboratory experiments can be described by a power law. We show that the corresponding exponent is related to roughness so that $\gamma = 3 - H$, where H is the Hurst exponent.

We conducted a second set of experiments at constant roughness revealing an approximately linear dependence of γ on normal stress. The combined influence of normal stress and roughness can explain the observed off-fault activity for all experiments. Our results substantiate previous findings suggesting a linear relationship between off-fault activity and roughness (Dieterich & Smith 2009; Powers & Jordan 2010). They also highlight the importance of the stress state on the fault in controlling seismicity distributions. For a comprehensive understanding of underlying mechanism of seismicity distributions the interplay between fault driving stresses and roughness has to be considered. The direct connection between off-fault seismicity exponents, fault stresses and roughness potentially allows for a direct mapping of fault zone properties based on microseismicity statistics, thus providing a tool for the understanding of the fault mechanics and local hazard potential.

ACKNOWLEDGEMENTS

We thank Stefan Gehrmann for the rock sample preparation at GFZ-Potsdam, Germany. We would like to thank Yehuda Ben-Zion for useful discussions that helped improve the data analysis. The manuscript benefited from the comments of an anonymous editor and reviewer. This research was supported in part by the Southern Californian Earthquake Center under contribution number 11017 and 13022.

REFERENCES

Amitrano, D. & Schmittbuhl, J., 2002. Fracture roughness and gouge distribution of a granite shear band, *J. geophys. Res.,* **107,** 2375.

Anders, M.H. & Wiltschko, D.V., 1994. Microfracturing, paleostress and the growth of faults, *J. Struct. Geol.,* **16**(6), 795–815.

Ben-Zion, Y. & Sammis, C.G., 2003. Characterization of fault zones, *Pure appl. Geophys.,* **160,** 677–715.

Brodsky, E.E., Gilchrist, J.J., Sagy, A. & Collettini, C., 2011. Faults smooth gradually as a function of slip, *Earth planet. Sci. Lett.,* **302**(1–2), 185–193.

Byerlee, J.D., 1970. The mechanics of stick-slip, *Tectonophysics,* **9**(5), 475–486.

Byerlee, J.D. & Brace, W.F., 1968. Stick slip, stable sliding, and earthquakes-effect of rock type, pressure, strain rate, and stiffness, *J. geophys. Res.,* **73**(18), 6031–6037.

Candela, T., Renard, F., Bouchon, M., Brouste, A., Marsan, D., Schmittbuhl, J. & Voisin, C., 2009. Characterization of fault roughness at various scales: implications of three-dimensional high resolution topography measurements, *Pure appl. Geophys.,* **166,** 1817–1851.

Candela, T., Renard, F., Bouchon, M., Schmittbuhl, J. & Brodsky, E.E., 2011a. Stress drop during earthquakes: effect of fault roughness scaling, *Bull. seism. Soc. Am.,* **101**(5), 2369–2387.

Candela, T., Renard, F., Schmittbuhl, J., Bouchon, M. & Brodsky, E.E., 2011b. Fault slip distribution and fault roughness, *Geophys. J. Int.,* **187**(2), 959–968.

Candela, T., Renard, F., Klinger, Y., Mair, K., Schmittbuhl, J. & Brodsky, E.E., 2012. Roughness of fault surfaces over nine decades of length scales, *J. geophys. Res.,* **117,** B08409, doi:10.1029/2011JB009041.

Chester, F.M. & Chester, J.S., 2000. Stress and deformation along wavy frictional faults, *J. geophys. Res.,* **105**(B10), 23 421–23 430.

Chester, F.M., Evans, J.P. & Biegel, R.L., 1993. Internal structure and weakening mechanisms of the San Andreas Fault, *J. geophys. Res.,* **98**(B1), 771–786.

Clauset, A., Shalizi, C.R. & Newmann, M.E.J., 2009. Power-law distributions in empirical data, *SIAM Rev.,* **51**(4), 661–703.

Dieterich, J., 1979. Modeling of rock friction – 1. Experimental results and constitutive equations, *J. geophys. Res.,* **84**(B5), 2161–2168.

Dieterich, J.H. & Kilgore, B.D., 1996. Imaging surface contacts: power law contact distributions and contact stresses in quartz, calcite, glass and acrylic plastic, *Tectonophys.,* **256**(1–4), 219–239.

Dieterich, J.H. & Smith, D.E., 2009. Nonplanar faults: mechanics of slip and off-fault damage, *Pure appl. Geophys.,* **166,** 1799–1815.

Feder, J., 1988. *Fractals,* Plenum Press.

Felzer, K.R. & Brodsky, E.E., 2006. Decay of aftershock density with distance indicates triggering by dynamic stress, *Nature,* **441,** doi:10.1038/nature04799.

Goebel, T. H.W., Becker, T.W., Schorlemmer, D., Stanchits, S., Sammis, C., Rybacki, E. & Dresen, G., 2012. Identifying fault hetergeneity through mapping spatial anomalies in acoustic emission statistics, *J. geophys. Res.,* **117,** B03310, doi:10.1029/2011JB008763.

Goebel, T. H.W., Sammis, C.G., Becker, T.W., Dresen, G. & Schorlemmer, D., 2013a. A comparision of seismicity characteristics and fault structure in stick-slip experiments and nature, *Pure appl. Geophys.,* doi:10.1007/s00024-013-0713-7, in press.

Goebel, T. H.W., Schorlemmer, D., Dresen, G., Becker, T.W. & Sammis, C.G., 2013b. Acoustic emissions document stress changes over many seismic cycles in stick-slip experiments, *Geophys. Res. Lett.,* **40,** doi:10.1002/grl.50507.

Griffith, W.A., Rosakis, A., Pollard, D.D. & Ko, C.W., 2009. Dynamic rupture experiments elucidate tensile crack development during propagating earthquake ruptures, *Geology,* **37**(9), 795–798.

Griffith, W.A., Nielsen, S., Toro, G.D. & Smith, S.A.F., 2010. Rough faults, distributed weakening, and off-fault deformation, *J. geophys. Res,* **115,** B08409, doi:10.1029/2009JB006925.

Hansen, A., Schmittbuhl, J., Batrouni, G.G. & de Oliveira, F.A., 2000. Normal stress distribution of rough surfaces in contact, *Geophys. Res. Lett.,* **27**(22), 3639–3642.

Hauksson, E., 2010. Spatial separation of large earthquakes, aftershocks, and background seismicity: analysis of interseismic and coseismic seismicity patterns in southern California, *Pure appl. Geophys.,* **167,** doi:10.1007/s00024-010-0083-3.

Huang, J. & Turcotte, D.L., 1988. Fractal distributions of stress and strength and variations of *b*-value, *Earth planet. Sci. Lett.,* **91,** 223–230.

Janssen, C., Wagner, F., Zang, A. & Dresen, G., 2001. Fracture process zone in granite: a microstructural analysis, *Int. J. Earth Sci.,* **90**(1), 46–59.

Kim, Y.-S., Peacock, D.C.P. & Sanderson, D.J., 2004. Fault damage zones, *J. Struct. Geol.,* **26**(3), 503–517.

Lockner, D., Byerlee, J., Kuksenko, V., Ponomarev, A. & Sidorin, A., 1991. Observations of quasistatic fault growth from acoustic emissions, in *Fault Mechanics and Transport Properties of Rocks,* pp. 3–31, eds Evans, B. & Wong, T.-F., Academic Press.

Main, I.G., Meredith, P.G. & Sammonds, P.R., 1992. Temporal variations in seismic event rate and *b*-values from stress corrosion constitutive laws, *Tectonophysics,* **211,** 233–246.

Mandelbrot, B., 1982. *The Fractal Geometry of Nature,* Freeman & Co.

McLaskey, G.C. & Glaser, S.D., 2011. Micromechanics of asperity rupture during laboratory stick slip experiments, *Geophys. Res. Lett.,* **38,** L12302, doi:10.1029/2011GL047507.

Mitchell, T. & Faulkner, D., 2009. The nature and origin of off-fault damage surrounding strike-slip fault zones with a wide range of displacements: a field study from the Atacama fault system, northern Chile, *J. Struct. Geol.,* **31**(8), 802–816.

Newman, M.E.J., 2005. Power laws, Pareto distributions and Zipf's law, *Contemp. Phys.,* **46**(5), 323–351.

Okubo, P. & Dieterich, J., 1984. Effects of physical fault properties on frictional instabilities produced on simulated faults, *J. geophys. Res.,* **89**(B7), 5817–5827.

Peng, Z. & Gomberg, J., 2010. An integrated perspective of the continuum between earthquakes and slow-slip phenomena, *Nat. Geosci.,* **3**(9), 599–607.

Persson, B. N.J., Albohr, O., Tartaglino, U., Volokitin, A.I. & Tosatti, E., 2005. On the nature of surface roughness with application to contact mechanics, sealing, rubber friction and adhesion, *J. Phys.: Condens. Matter,* **17**(1), R1–R62.

Power, W.L. & Durham, W.B., 1997. Topography of natural and artificial fractures in granitic rocks: implications for studies of rock friction and fluid migration, *Int. J. Rock. Mech. Min. Sci.,* **34,** 979–989.

Power, W.L., Tullis, T.E., Brown, S.R., Boitnott, G.N. & Scholz, C.H., 1987. Roughness of natural fault surfaces, *Geophys. Res. Lett.,* **14,** 29–32.

Powers, P.M. & Jordan, T.H., 2010. Distribution of seismicity across strike-slip faults in California, *J. geophys. Res.,* **115,** doi:10.1029/2008JB006234.

Rathbun, A.P., Renard, F. & Abe, S., 2013. Numerical investigation of the interplay between wall geometry and friction in granular fault gouge, *J. geophys. Res.,* **118,** doi:10.1002/jgrb.50106.

Renard, F., Candela, T. & Bouchaud, E., 2013. Constant dimensionality of fault roughness from the scale of micro-fractures to the scale of continents, *Geophys. Res. Lett.,* **40,** 83–87.

Rockwell, T.K. & Ben-Zion, Y., 2007. High localization of primary slip zones in large earthquakes from paleoseismic trenches: observations and implications for earthquake physics, *J. geophys. Res.,* **112**(B10), B10304, doi:10.1029/2006JB004764.

Sagy, A., Brodsky, E.E. & Axen, G.J., 2007. Evolution of fault-surface roughness with slip, *Geology,* **35,** 283–286.

Sammis, C.G. & Steacy, S.J., 1994. The micromechanics of friction in a granular layer, *Pure appl. Geophys.,* **142**(3–4), 777–794.

Sammonds, P. & Ohnaka, M., 1998. Evolution of microseismicity during frictional sliding, *Geophys. Res. Lett.,* **25,** 699–702.

Savage, H.M. & Brodsky, E.E., 2011. Collateral damage: evolution with displacement of fracture distribution and secondary fault strands in fault damage zones, *J. geophys. Res.,* **116**(B3), doi:10.1029/2010JB007665.

Schmittbuhl, J., Chambon, G., Hansen, A. & Bouchon, M., 2006. Are stress distributions along faults the signature of asperity squeeze?, *Geophys. Res. Lett.,* **33**(13), L13307, doi:10.1029/2006GL025952.

Scholz, C.H., 1968. The frequency-magnitude relation of microfracturing in rock and its relation to earthquakes, *Bull. seism. Soc. Am.,* **58,** 399–415.

Silverman, B.W., 1986. *Density Estimation for Statistics and Data Analysis,* Chapman and Hall.

Stesky, R.M., 1978. Mechanisms of high temperature frictional sliding in Westerly granite, *Can. J. Earth Sci.,* **15,** 361–375.

Tsallis, C. & Brigatti, E., 2004. Nonextensive statistical mechanics: a brief introduction, *Contin. Mech. Thermodyn.,* **16**(3), 223–235.

Turcotte, D.L., 1997. *Fractals and Chaos in Geology and Geophysics,* Cambridge Univ. Press.

Vallianatos, F., Benson, P., Meredith, P. & Sammonds, P., 2012. Experimental evidence of a non-extensive statistical physics behaviour of fracture in triaxially deformed Etna basalt using acoustic emissions, *Europhys. Lett.,* **97**(5), doi:10.1209/0295-5075/97/58002.

Vallianatos, F., Michas, G., Benson, P. & Sammonds, P., 2013. Natural time analysis of critical phenomena: the case of acoustic emissions in triaxially deformed Etna basalt, *Physica A: Stat.Mech. Appl.,* **392**, 5172–5178.

Wechsler, N.Y. & Ben-Zion Christofferson, S., 2010. Evolving geometrical heterogeneities of fault trace data, *Geophys. J. Int.,* **182**(2), 551–567.

Wesnousky, S.G., 1988. Seismological and structural evolution of strike-slip faults, *Nature,* **335,** 340–342.

Xu, S.Y. & Ben-Zion, 2013. Numerical and theoretical analyses of in-plane dynamic rupture on a frictional interface and off-fault yielding patterns at different scales, *Geophys. J. Int.,* **193**(1), 304–320.

Zang, A., Wagner, F.C., Stanchits, S., Janssen, C. & Dresen, G., 2000. Fracture process zone in granite, *J. geophys. Res,* **105**(B10), 23 651–23 661.